nature materials

Article

https://doi.org/10.1038/s41563-025-02373-w

Unisensory processing of interleaving memristive nanowires enabling multimodal sensing at human-scale resolution

Received: 5 April 2024

Accepted: 9 September 2025

Published online: 24 October 2025

Check for updates

Kyun Kyu Kim[1,2,5], Junhyuk Bang[2,5], Munju Kim[2], Juho Jeong[2], Inho Ha[2] & Seung Hwan Ko[2,3,4]

Numerous attempts have been made to emulate the skin's multimodal capabilities using different device architectures, but most suffer from slow response due to reactive components and limited scalability from stacking multiple elements, which restricts their practical use. Here we report a multimodal receptor based on a single memristive nanowire network that captures both thermal and mechanical properties of interacting objects through memristive switching. The device switches between thermal and mechanical sensing at 16 Hz, whereas its intrinsic response times reach submicrosecond (mechanical) and millisecond (thermal) levels due to the nanoscale thickness. To demonstrate practicality, we integrated the receptor with a wireless switching board for daily use, combined it with a machine learning model to identify 20 household objects with 83% accuracy using a single fingertip-mounted sensor, and performed multiarray measurements for spatially distributed sensing. This approach highlights the potential of memristive networks for compact and versatile multimodal sensing in wearable and interactive devices.

Sensory neurons exhibit multimodality, playing a crucial role in the efficient and robust processing of signals to create a comprehensive representation of the external environment[1,2]. Temperature and pressure stimuli on the skin, in particular, serve as vital cues for discerning the texture and shape of interacting objects[3,4]. For accurate and immediate perception, the spatiotemporal resolution of a sensory receptor is imperative, enabling the central nervous system to rapidly process intricate stimuli applied on the skin[5,6].

Numerous attempts have been made to emulate the skin's multimodal capabilities. Predominantly, these efforts have involved integrating independent sensing elements for measuring the temperature and pressure[7–9]. This approach, however, necessitates a substantial systemic complexity to accommodate multiple materials and external measuring units, resulting in a compromised areal resolution (Fig. 1a). Although some progress has been made towards integrating multimodality within a single sensory element, the prevalent strategies often rely on decoupling reactive components from ionic materials[10,11] and microdome structures[12,13], which inherently introduces response delays.

By contrasting previous strategies, we introduce a novel multimodal receptor, preserving multimodal information via fluctuating signals—a principle echoing the technique in telecommunications in which encoding multiple data within a constrained channel capacity is vital[14]. Such interleaving mechanisms, hypothesized to be operational within the nerve system[15–19] (Fig. 1b), have garnered experimental support[20] from observed single-neuron switching behaviour.

Our design leverages the unique properties of stretchable memristive nanowire networks, featuring switchable connectivity pathways of

[1]Department of Chemical Engineering, Stanford University, Stanford, CA, USA. [2]Department of Mechanical Engineering, Seoul National University, Seoul, Republic of Korea. [3]Institute of Advanced Machinery and Design (SNU-IAMD)/Institute of Engineering Research, Seoul National University, Seoul, Republic of Korea. [4]Interdisciplinary Program in Bioengineering, Seoul National University, Seoul, Korea. [5]These authors contributed equally: Kyun Kyu Kim, Junhyuk Bang. e-mail: maxko@snu.ac.kr

https://doi.org/10.1038/s41563-025-02373-w

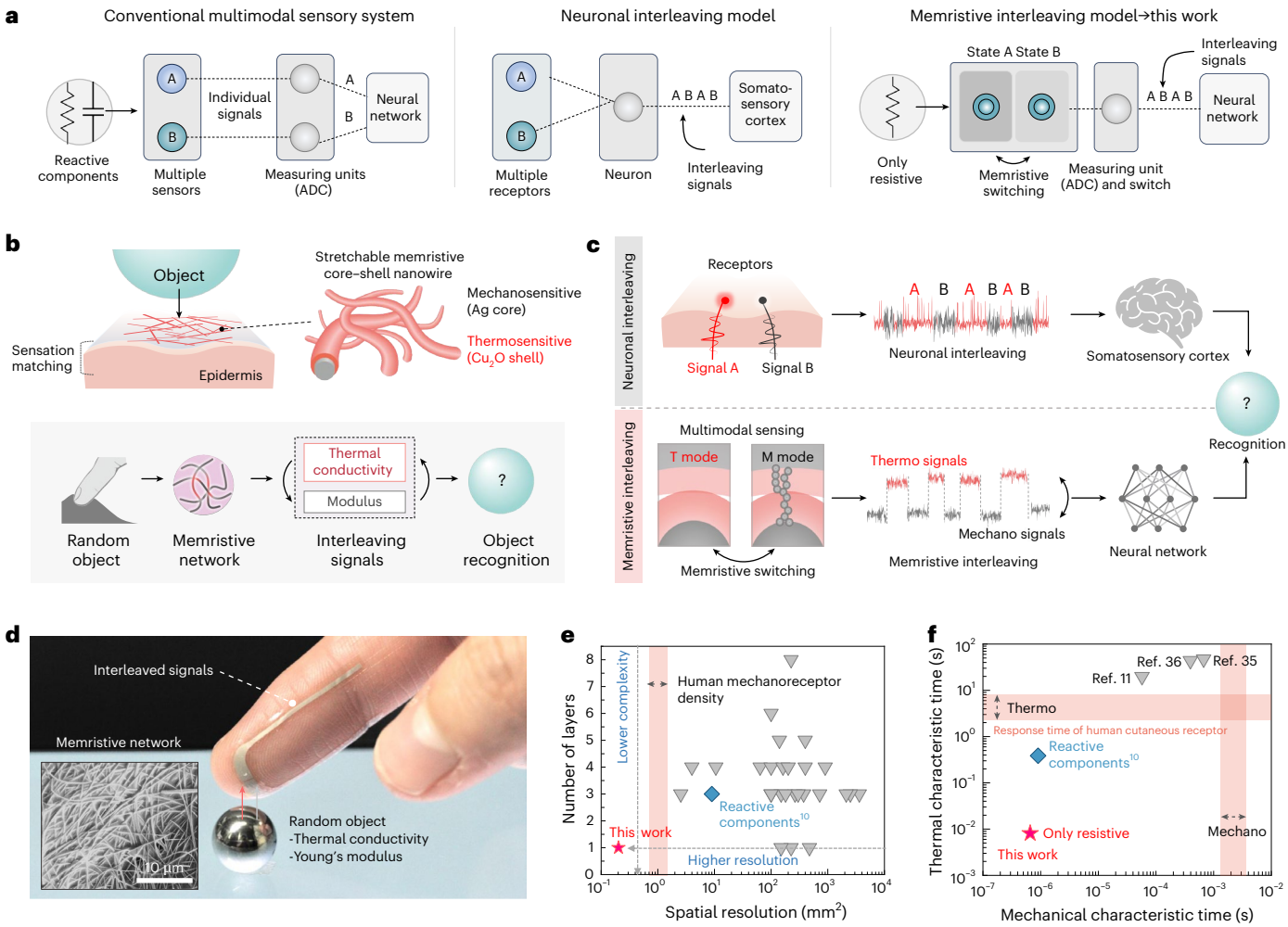

Fig. 1 | Artificial multimodal receptor. a, Schematic comparing a conventional multimodal sensory system alongside a neural interleaving model and our memristive interleaving model. Unlike the conventional system that requires independent measuring units for each modality, our system, inspired by the neural interleaving model, acquires multimodal information using a single measuring unit. **b**, Schematic of an interleaving memristive nanowire network sensor. **c**, Drawing inspiration from biological systems in which neurons interleave multiple signals before transmitting to the somatosensory cortex, memristive switching of our multimodal receptor's sensing modes interleave thermomechanical signals before relaying them to a neural network. **d**, Multimodal receptor, conformally attached to the skin, captures the inherent thermal and mechanical properties of random objects. Inset: memristive nanowire network on a skin replica with a magnified view via scanning electron microscopy. **e**,**f**, Comparison of the present study with preceding studies in terms of the number of active layers and areal resolution[7,9–13,28–52] (**e**) and characteristic time of heat transfer and mechanical deformation (**f**).

shell and core (Fig. 1c). By utilizing the inherent sensitivity of the incorporated materials and network geometry, we have successfully created distinct sensory states during the switching process. This design allows the selective extraction of temperature and strain signals in a singular resistance profile, which is correlated to the inherent material properties governed by the thermal conductivity and the modulus (Fig. 1d).

The absence of other reactive components in our design ensures a rapid response of sensation, moving us closer to achieving an emulation of the skin's sensory efficiency. External voltage is applied to transition between memristive states in the nanowire, with the Cu_2O shell representing the thermosensitive mode (T mode) and the Ag core corresponding to the mechanosensitive mode (M mode). A deep neural network is subsequently used to interlace these memristor states, enabling precise material classification.

Our design not only incorporates a fast response time but also exhibits a high spatial resolution. The single-layer sensor is capable of simultaneously detecting multiple inputs at the same location, addressing a key limitation of previous works in which multiple sensors were laterally patterned, preventing the measurement of signals from an identical region. Although some prior studies used stacked sensor architectures to enable multimodal detection, these designs often suffer from mechanical or thermal sensing delays due to increased thickness, an issue that our single-layer design inherently avoids.

As a result, the single-layer core–shell nanowire network provides a higher sensing unit resolution than previous solutions (Fig. 1e and Supplementary Tables 1 and 2). Additionally, the submicrometre-scale thickness of our nanowire network facilitates quicker thermal and mechanical responses (Fig. 1f). These findings mark an instance of surpassing both mechanical and thermal resolutions of human receptors, setting a new benchmark in the field.

Dynamic switching of sensing mode with computational analysis

The proposed sensor integrates a silver nanowire (AgNW) electrode with an $Ag@Cu_2O$ core–shell nanowire as the interleaved sensing layer. Other material candidates, such as Ag@polyvinylpyrrolidone and $Cu@Cu_2O$, we conducted additional experiments to evaluate the memristive performance of this material. Ag@polyvinylpyrrolidone material shows poor retention, indicating that it is unstable for use as a memristive switching material. Furthermore, $Cu@Cu_2O$ materials

https://doi.org/10.1038/s41563-025-02373-w

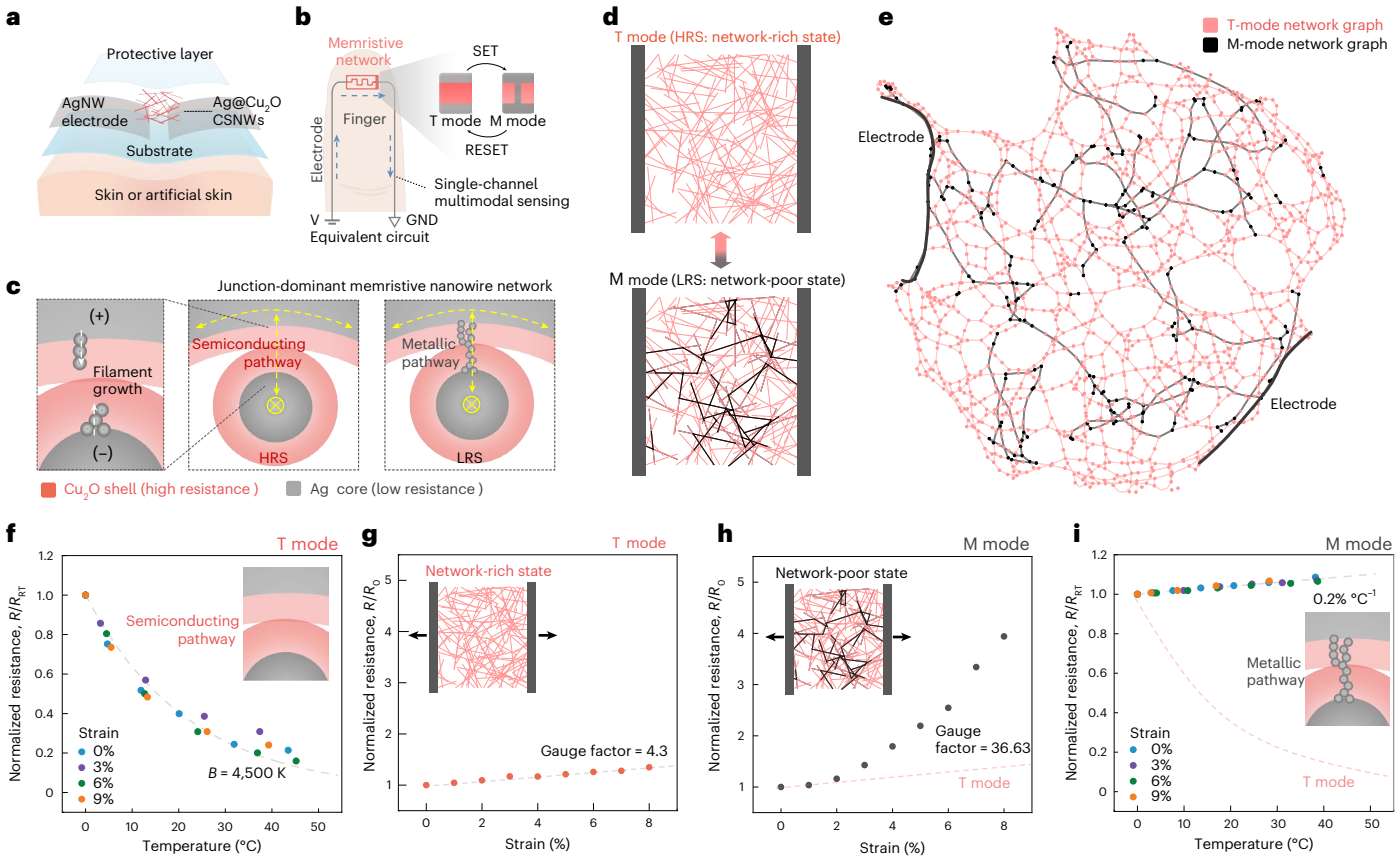

Fig. 2 | Dynamic switching of sensing mode. a, Schematic depicting the layered assembly of our multimodal receptor with core–shell nanowires (CSNWs). **b**, An equivalent circuit representation of our sensor system, which acquires multimodal information individually through a single-channel architecture. **c**, Schematic illustrating the memristive behaviour during switching between the HRS and LRS at the nanowire junctions. The charge-carrying material transitions from a semiconducting (Cu_2O shell) to a metallic (conductive filament) state. **d**, During the switching between the T and M modes of the memristive nanowire network, there is a change in the network geometry. In the M mode, the electrodes at either end are connected through a poor network. **e**, An undirected graph of computational results in the switching dynamics of the memristive nanowire network shows the differences in network density at the T and M modes. **f**,**g**, Response of the normalized resistance in the T mode to temperature change (**f**) and strain change (**g**). **h**,**i**, Response of the normalized resistance in the M mode to strain change (**h**) and temperature change (**i**).

shows memristive switching performance; however, during repetitive cycling, the SET curves exhibit inconsistencies with multilevel variances (Supplementary Fig. 1).

Ag@Cu_2O core–shell nanowires are patterned on a stretchable polydimethylsiloxane substrate, encapsulated with a protective layer for enhanced durability (Fig. 2a and Supplementary Fig. 2). The T-mode and M-mode states are achieved through a programmed voltage pulse delivered to the electrodes. This process enables the capture of interleaved signals by measuring the resistance during the distinct switching states (Fig. 2b).

The intrinsic multimodality of this sensor is attributed to the dynamic switching mechanism of the memristive nanowires, which is driven by the connections and disconnections of filaments within the nanowires. As shown in Fig. 2c, the Cu_2O shell initially forms a high-resistance state (HRS), where it also serves as a high-thermal-sensitivity material[21]. However, on applying a certain voltage pulse, a conductive filament forms by migrating metal ions across the Cu_2O layer connecting the Ag cores, resulting in a transition to the low-resistance state (LRS). When a high current flows, a conductive filament collapses and returns to the disconnected state—the HRS.

Furthermore, the distinction between the M and T modes is amplified by the unique nanowire network geometry (Fig. 2d). In the T mode (or the HRS state), connections span across the Cu_2O shell network. However, in the M mode (or the LRS state), connections are optimized for the shortest conductive pathway, leading to fewer overall connections (represented by the black lines). This sparse network connection augments its mechanical sensitivity, clearly distinguishing the differences between the T and M modes[22].

A computational model that describes memristive switching dynamics has been developed (detailed in Methods and Supplementary Figs. 24 and 25). Incorporating Kirchhoff's theory into a graph model provides insights into the network connections distinguishing the T mode from the M mode (Fig. 2e).

Figure 2f–i demonstrates the distinctive outputs resulting from each switching state. The T mode, predominantly governed by the p-type Cu_2O shell, exhibits high thermal sensitivity (Fig. 2f). The resulting experimental resistance profiles for the M and T modes under strain and temperature closely align with the simulation values (Supplementary Fig. 3).

The thermistor material constant for the T mode is deduced to be 4,500 K (within a measurement range of 25–65 °C) following the equation, $R = R_\infty e^{B}/T$. Even under 8% tensile strain, this sensitivity remains consistent, attributed to the nanowire's percolative network. Concurrently, the T mode's mechanical sensitivity under 8% strain shows a modest rise in resistance (Fig. 2g).

By contrast, the M mode, characterized by its limited network connections, shows high mechanical sensitivity with a gauge factor of 36 (Fig. 2h). In circumstances where fracture occurs during the

https://doi.org/10.1038/s41563-025-02373-w

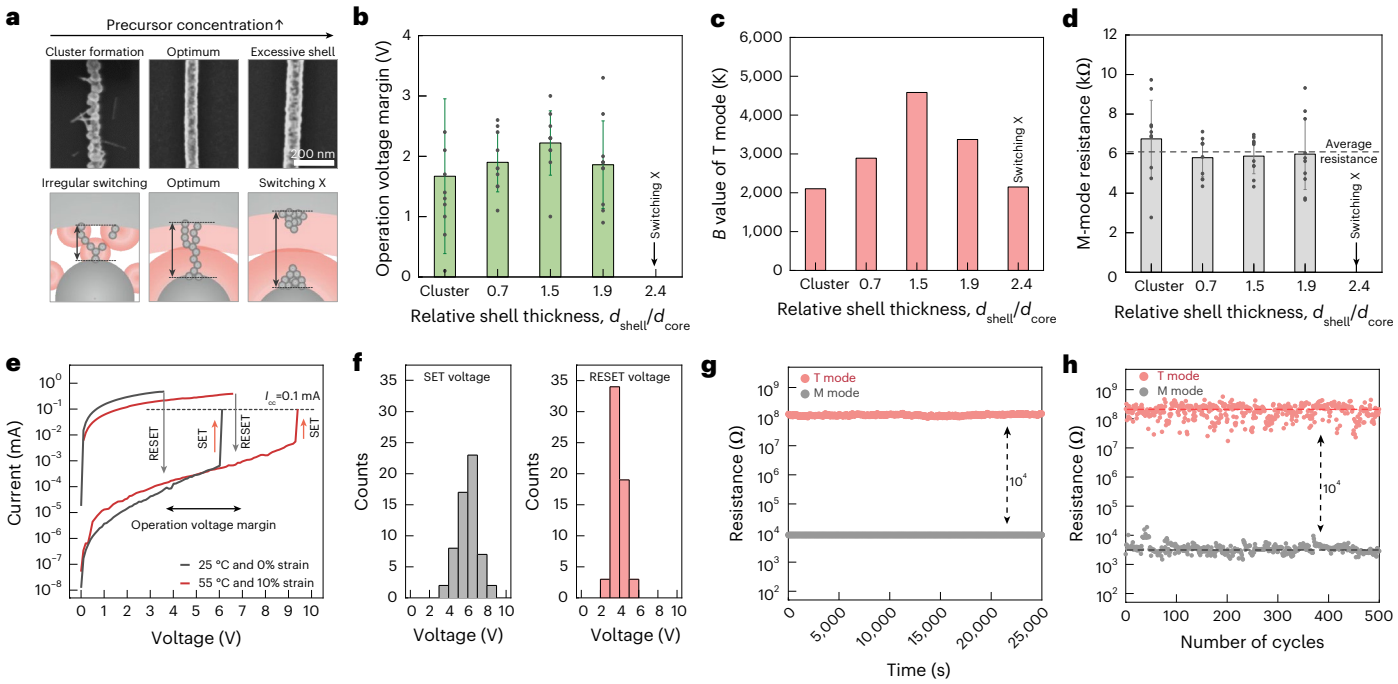

Fig. 3 | Characterizations of memristive multimodal receptor. a, Scanning electron microscopy images of Ag@Cu_2O core–shell nanowires at varying precursor concentrations, alongside schematics of the memristive switching behaviour influenced by the shell morphology. Comparative analysis of control and sensing characteristics to the RST. **b**, Operation voltage margin. Data are represented as mean ± standard deviation (s.d.; $n = 10$). Error bars represent the s.d. **c**,**d**, *B* value in the T mode (**c**) and resistance in the M mode (**d**). Data are represented as mean ± s.d. ($n = 10$). Error bars represent the s.d. **e**, Switching characteristics of our multimodal receptor, showcasing a unipolar switching effect. **f**, Histogram of SET and RESET voltages during memristive switching (59 samples), both following a Gaussian distribution. **g**, Retention time of T and M modes under a bias voltage of 1.5 V. **h**, Endurance characteristics of a memristive nanowire network undergoing over 500 switching cycles.

M mode, switching back from HRS to LRS ensures reconnection of the disconnected filaments, restoring the resistance to the value (Supplementary Fig. 4).

Furthermore, it demonstrates thermal insensitivity due to the AgNW's lower temperature coefficient of resistance (0.2 $°C^{-1}$)[23] (Fig. 2i). Contour plots derived from experimental data in the T and M modes show nearly vertical alignment between each state. This indicates that strain and temperature values can be accurately extracted from the intersection points of the two contour plots. This ensures that despite the inherent coupling, the resolution and performance of the sensor are maintained by enabling a precise separation of the effects of strain and temperature (Supplementary Fig. 5).

Analysis of memristive multimodal receptor characteristics

The memristive and multimodal properties of the Ag@Cu_2O nanowire sensor can be tuned by adjusting the shell thickness. The goal is to determine the best difference in supply voltage to enable a clear transition between SET (M mode) and RESET (T mode). Additionally, a Cu_2O shell thickness affects the temperature sensitivity, necessitating a precise adjustment of the shell's thickness. This adjustment is achieved by varying the concentration of the $CuCl_2$ precursor solution; a higher concentration results in a thicker Cu_2O shell (Supplementary Fig. 6), whereas an excessively low concentration causes irregular Cu_2O clusters to form on the AgNW surface (Fig. 3a).

The Cu_2O shell thickness influences the switching characteristics when applying the SET (M mode) and RESET (T mode) voltages (Supplementary Fig. 7)[24]. A low relative shell thickness (RST = d_{shell}/d_{core}) leads to a smaller voltage difference between the modes with higher variability, which compromises the control over switching (Fig. 3b). The best control and the widest voltage margin occur at an RST of 1.5. However, if the RST is too high, this state cannot be switched due to the shell's excessive thickness, even under 35 V.

For relative thicknesses (d_{shell}/d_{core}) greater than 1.5, the longer ion migration distances introduce a higher energy barrier for filament dissolution, resulting in a higher RESET voltage and lower operation voltage margin. RST values below 0.7 unexpectedly exhibit higher SET and RESET voltages. This discrepancy arises from incomplete shell formation during synthesis and creating clusters. In such cases, the clusters prevent current flow, necessitating a higher voltage input to establish a sufficient voltage gradient between the memristive layer and core material (Supplementary Fig. 8).

Thermal sensitivity in the T mode peaks at an RST of 1.5 (with a *B* value of 4,500 K), but thermal sensitivity decreases when the shell is too thick, as resistance increases excessively due to the semiconducting nature of the Cu_2O layer (Fig. 3c)[25]. Here scattering effects are introduced, which dominate over thermally activated conduction, diminishing the impact of temperature changes on the overall conductivity and resulting in a lower *B* value. Figure 3d shows that the electrical resistance of the M mode remains stable over a range of RST values, which indicates that the mechanical sensitivity is constant. An RST value of 1.5 is ideal for maximizing control, thermal sensitivity and mechanical sensitivity.

Figure 3e demonstrates that our sensor can reliably switch between the T and M modes, even under challenging conditions such as heating to 55 °C and applying a 10% tensile strain. There's a considerable margin in operational voltage, which helps maintain control over switching between the states even when the sensor is under heat and mechanical stress.

Moreover, the consistency in the SET and RESET voltages across 59 samples, which show a normal distribution, attests to the uniformity of our manufacturing process (Fig. 3f). This is consistent under different

densities for the nanowire, where Monte Carlo simulation results align closely with the experimental observations (Supplementary Fig. 9).

Our sensor also exhibits high durability and consistent performance, maintaining a significant on/off ratio of 10,000. This reliability is maintained over extended periods, demonstrated by over 7 h of continuous measurement at a bias voltage of 1.5 V and through 500 cycles of repeated switching (Fig. 3g,h).

Predicting objects via interleaved measurement of thermal and mechanical properties

The developed memristive sensor emulates the human sensory system's ability to perceive fundamental material properties on initial contact. The sensor's thin profile enables it to rapidly align with the object's temperature profile, whereas the thick sensor shows a more gradual response, indicating slower thermal and mechanical responsiveness (Supplementary Figs. 10 and 11). As illustrated in Fig. 4a, the sensor is designed to discern between heat flux and material stiffness, which are influenced by the material's thermal conductivity and modulus, respectively. High-thermal-conductivity materials exhibit a rapid temperature response, where such materials cause a quick increase in temperature on contact. Similarly, materials with a higher Young's modulus are characterized by larger depth under a given indentation force, demonstrating their stiffness. The developed memristive sensor allows it to record these temporal responses to both temperature changes and mechanical pressures as a distinct resistance change.

Control experiments further support that there is no signal interference between the two modes (Supplementary Fig. 12). When touching a heated object (45 °C) without applying compressive pressure, thermal transfer is isolated and only the T mode is activated (Fig. 4b). By contrast, when pressure is applied without a temperature gradient, only the M mode responds to the indentation force (Fig. 4c).

To better understand the capabilities of our sensor system, we experimented with four distinct materials (Fig. 4d), each possessing unique thermal conductivity and modulus values (Supplementary Fig. 13). We postulate that information regarding the modulus will be captured by the M mode, whereas insights into thermal conductivity will be derived from the T-mode values (Supplementary Fig. 14). Subsequently, by feeding these interleaved signals (Supplementary Fig. 15) into a machine learning network, we can identify the material class. In Fig. 4e, the interleaving phases are demonstrated, showcasing the consistent differentiation between the T and M modes throughout a complete contact cycle.

To capture the temporal sequences of the interleaved states between the M and T modes, we used a long short-term memory (LSTM) network (Fig. 4f and Supplementary Fig. 16). The decoding network, which translates latent vectors to specific points in our two-dimensional metric space, consists of dense layers. Following this, the vector generated by the LSTM with the attention block is concatenated with the original input, ensuring retention of the signal's inherent information. Finally, the dense layers transform the encoded latent vectors into distinct object classes. A comprehensive outline of the model architecture is provided in Methods.

To visualize and evaluate the results of the trained dataset, we applied *t*-distributed stochastic neighbour embedding (*t*-SNE)[26]. The *t*-SNE visualization reveals well-defined clusters in the projected two-dimensional space, providing insights into the relationships between samples and the separability of classes in high-dimensional space. *t*-SNE distinctly presents signals associated with object classes (Fig. 4g–i).

For a comparative analysis of our sensing system's information-rich attributes, we deliberately gathered solely M-mode and T-mode signals from Ag and Ag@Cu_2O nanowires, respectively. Figure 4g,h shows the embedded signal vectors in which object classes seem to be entangled and indistinct. By contrast, Fig. 4i clearly differentiates object classes, underscoring that our interleaved sensory system captures both mechanical and thermal information that facilitates precise material-class recognition.

Figure 4j shows the accuracy of object identification provided by interleaved signals over single-modality signals. When utilizing solely mechanical or thermal signals, the accuracy saturated at 65%, indicating a limitation when these modalities are used in isolation. Conversely, the interleaved approach, which integrates both thermal and mechanical information, significantly improved accuracy, reaching 95% with the same number of training epochs.

The interplay between the amount of data and identification accuracy is further explored in Fig. 4k. Stand-alone mechanical or thermal datasets, each with 1,273 data points, yielded a 65% accuracy rate. However, when these datasets were combined, harnessing the full spectrum of 1,273 data points for both thermal and mechanical signals, the accuracy reached 97%. In particular, the interleaved dataset, which incorporated both thermal and mechanical signals but with only half the number of data points (636), achieved a 94.53% accuracy rate. This result is comparable with the accuracy obtained using the full dataset. This evidence clearly demonstrates the computational efficiency of our interleaved sensing system, which maintains high accuracy even with a reduced dataset size. This is not only advantageous in terms of computational resources but also indicates the robustness of the sensing approach. The effectiveness of our sensor system in distinguishing between different objects is visually depicted in a confusion matrix (Fig. 4l).

Interaction with diverse objects and human-scale resolution array

Figure 5a depicts the process of the in-sensor interleaving mechanism for capturing thermomechanical information during tactile interaction. Our system seamlessly alternates between the T and M modes, producing two distinct signals that represent the thermal and mechanical properties of the object (Supplementary Fig. 17). We extended our results to classify a greater variety of objects by developing a portable wireless module. This module enables effective and stable signal transmission during user interaction with objects, without interrupting the user's movement (Supplementary Fig. 18).

Figure 5b illustrates the incorporation of a current-limiting diode to set compliance currents for the SET (0.1 mA) and RESET (3 mA) states. Four transistors are actively connected to switch between these states, where V_1 controls the gate voltage for SET, V_2 for RESET, V_3 for T-SENSE after the RESET mode and V_4 for M-SENSE after the SET mode. The detailed programming logic is presented in Fig. 5c. During transitions from the T-SENSE state to the M-SENSE mode, a 5-ms switching pulse is triggered for voltage sweeping, whereas a low voltage is applied between these steps to monitor resistance variance. Once the resistance drops significantly, the SET mode is completed, and the system transitions to the M-SENSE mode for resistance measurement. The RESET mode operates in the same logic during contact (Supplementary Video 1).

The developed wireless measurement board is illustrated in Fig. 5d. It features a digital-to-analogue converter connected through an amplifier to the sensor network for voltage input. The transistors actively switch states, with current regulated by a current-limiting diode. The voltage is divided by the reference resistor, and the analogue measurements are transmitted via Bluetooth Low Energy communication. With the integration of the wireless board and sensor, efficient dataset collection of 20 objects (Supplementary Fig. 19) is enabled. As shown in Fig. 5e,f, *t*-SNE visualization and per-class accuracy demonstrate an overall validation accuracy of 83% (Supplementary Fig. 20). In particular, this performance is achieved using a unisensory platform, highlighting the synergistic functionality of the sensor and the wireless module for effective data transfer during interactions.

The ultrathin material and single-layer design allow scalability into multiarray configurations, achieving resolutions comparable with

https://doi.org/10.1038/s41563-025-02373-w

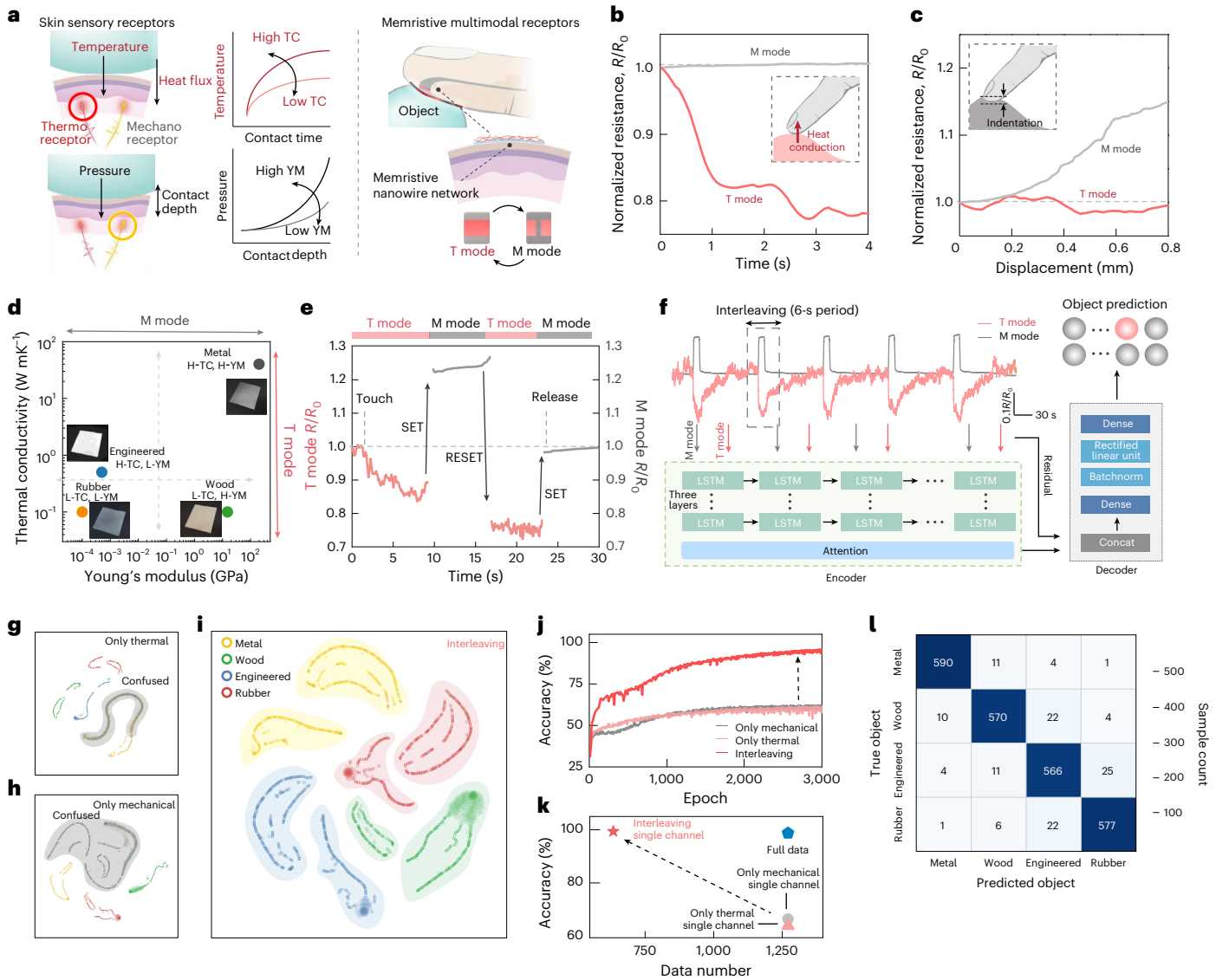

Fig. 4 | Object recognition using interleaved signals. a, Comparison of human cutaneous receptor and our multimodal receptor. Our multimodal receptor replicates human cutaneous receptors, which perceive indentation and temperature changes according to the physical properties of the object. **b**, Normalized resistance of our multimodal sensor over contact time with a heated material. **c**, Normalized resistance of our multimodal sensor according to contact depth. **d**, Group of recognition objects (wood, metal, rubber and engineered) along with their respective thermal conductivity (TC) and Young's modulus (YM). **e**, Illustration of multiple sensing modes transitioning throughout a complete contact cycle. **f**, Detailed learning structure including an LSTM encoder with an attention block; the decoder consists of dense layers. **g**–**i**, *t*-SNE visualization representing object differentiation using only thermal (**g**), only mechanical (**h**) and combined interleaved signals (**i**). **j**, Comparative analysis of classification accuracy using only thermal, only mechanical and combined interleaved signals. **k**, Demonstration that interleaved signals achieve similar accuracy to the full thermal and mechanical datasets with a smaller data volume. Sole thermal or mechanical signals exhibit lower classification accuracy. **l**, Confusion matrix illustrates the accuracy of object classification using interleaved signals.

human perception (Fig. 5g)[27]. To further demonstrate this capability, we developed a multiarray sensing platform using a custom-made board to multiplex incoming signals (Supplementary Fig. 21). Figure 5h shows the developed multiarray platform. As illustrated in Fig. 5i, a T-shaped block with a corrugated microheater pattern made of AgNWs generates heat in a T-shaped profile. The multiarray sensor successfully translates this temperature profile in the T mode. Similarly, in Fig. 5j, an M-shaped block is applied to the sensor array, and the resulting M-shaped pressure distribution is accurately measured, as shown in Fig. 5k (Supplementary Video 2).

Outlook

In this study, we have successfully designed a multimodal sensor capable of simultaneously detecting mechanical and thermal stimuli using a singular sensory element through the implementation of memristive nanowire network switching. This approach facilitates unisensory processing, significantly simplifying the system architecture by necessitating only one type of sensory output. Crucially, the absence of reactive components in our design allows for rapid sensory responses, bringing us a step closer to mimicking the efficiency of human skin's sensory system. The ultrathin material and single-layer design of our sensor support scalability into multiarray configurations, achieving resolutions comparable to human perception. This scalability provides the ability to gather high-resolution sensory data at a human scale. We have engineered and computationally validated the memristive network's ability to actively switch between the T-mode and M-mode states. The development of a wireless switching module seamlessly connected to the sensor enables direct signal transfer to the deep neural network, integrating memristor states to achieve precise and high-capacity

https://doi.org/10.1038/s41563-025-02373-w

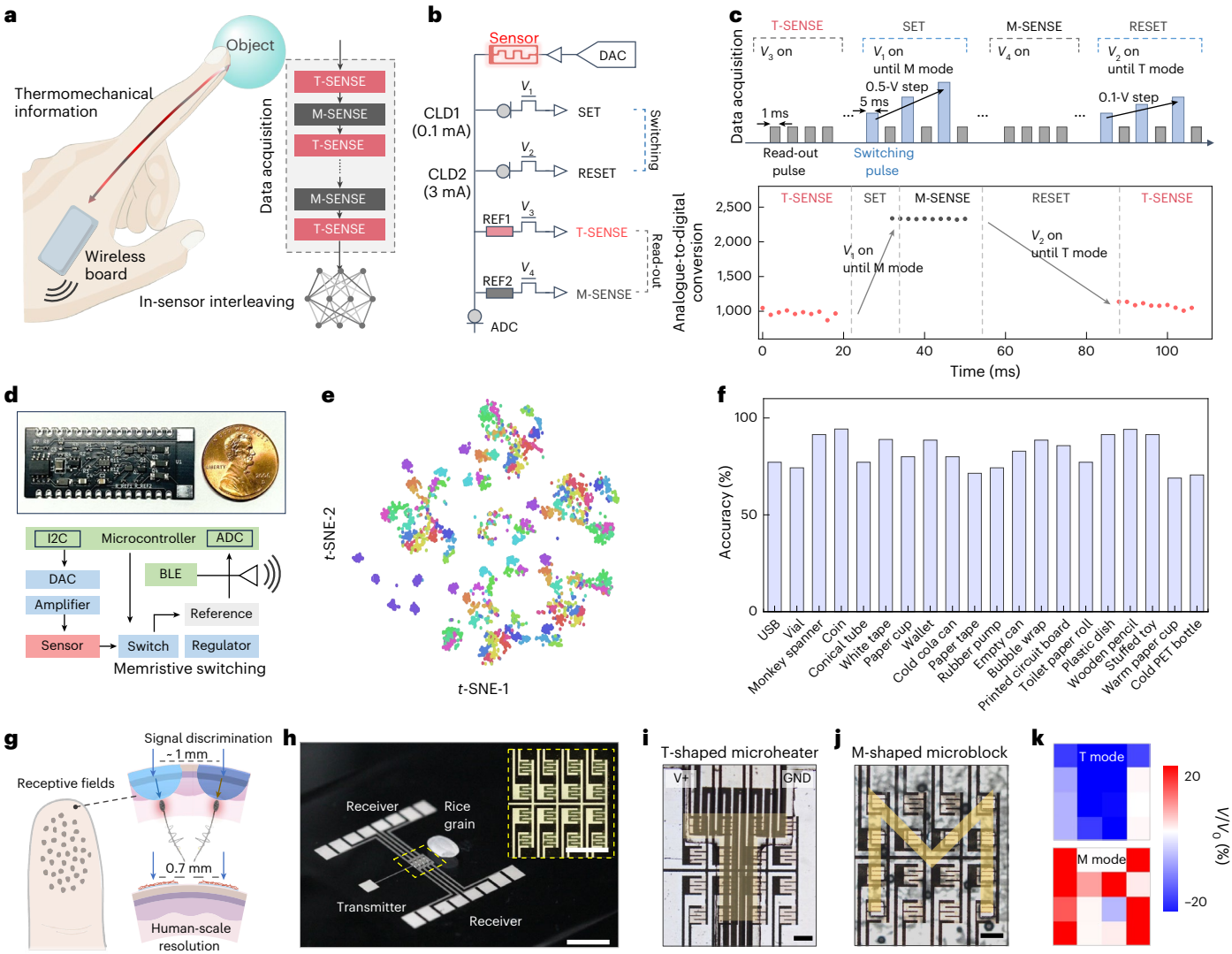

Fig. 5 | Integration with autonomous switching board and human-scale multiarray measurement. a, Wireless switching module that connects seamlessly to the sensor, enabling direct signal transfer to the learning network. **b**, Electrical schematic of the module. Incorporation of a current-limiting diode to set compliance currents and four transistors to control the gate voltage. DAC, digital-to-analogue converter; ADC, analogue-to-digital converter. **c**, Sensing scheme of T-SENSE and M-SENSE and the corresponding measurement. The reading frequency is set to 500 Hz and the switching frequency, to 16 Hz. Within each 1-s period, M-SENSE and T-SENSE alternated, with eight cycles assigned to each mode. **d**, Picture and diagram of the autonomous switching wireless sensing module. BLE, Bluetooth Low Energy; I2C, inter-integrated circuit. **e**, *t*-SNE plot of the classified 20 objects. **f**, Per-class validation accuracy among 20 objects. The dataset is divided into training and validation datasets with a ratio of 8:2. **g**, Resolution of the receptive field of the skin compared with the developed sensor. **h**, Image of the developed multiarray device. Scale bar, 5 mm; 1 mm (inset). **i**,**j**, T-shaped block (**i**) and M-shaped block (**j**) placed on top of the device. Scale bars, 500 μm. **k**, Measured T-shaped and M-shaped blocks through active T-mode and M-mode switching.

material classification. The varied demonstrations of our sensor's ability to distinguish between different material properties underscore its broad applicability. Although our system demonstrates robust performance, future improvements could be achieved by implementing on-device signal processing, taking advantage of interleaved signals with lower memory requirements. Additionally, expanding the dataset to incorporate multiarray signals would enhance the richness of material information, enabling greater adaptability for the recognition of a wider range of materials. This technology shows great promise for integration into a diverse array of fields, including prosthetics, wearables and soft robotics.

Online content

Any methods, additional references, Nature Portfolio reporting summaries, source data, extended data, supplementary information, acknowledgements, peer review information; details of author contributions and competing interests; and statements of data and code availability are available at https://doi.org/10.1038/s41563-025-02373-w.

References

1. Stein, B. E. & Stanford, T. R. Multisensory integration: current issues from the perspective of the single neuron. *Nat. Rev. Neurosci.* **9**, 255–266 (2008).
2. Follmann, R., Goldsmith, C. J. & Stein, W. Multimodal sensory information is represented by a combinatorial code in a sensorimotor system. *PLoS Biol.* **16**, e2004527 (2018).
3. Ho, H.-N. & Jones, L. A. Contribution of thermal cues to material discrimination and localization. *Percept. Psychophys.* **68**, 118–128 (2006).
4. Takamuku, S., Iwase, T. & Hosoda, K. Robust material discrimination by a soft anthropomorphic finger with tactile and thermal sense. In *2008 IEEE/RSJ International Conference on Intelligent Robots and Systems* 3977–3982 (IEEE, 2008).

5. Johansson, R. S. & Flanagan, J. R. Coding and use of tactile signals from the fingertips in object manipulation tasks. *Nat. Rev. Neurosci.* **10**, 345–359 (2009).
6. Bensmaia, S. J. Biological and bionic hands: natural neural coding and artificial perception. *Philos. Trans. R. Soc. Lond. B Biol. Sci.* **370**, 20140209 (2015).
7. Wu, X., Zhu, J., Evans, J. W., Lu, C. & Arias, A. C. A potentiometric electronic skin for thermosensation and mechanosensation. *Adv. Funct. Mater.* **31**, 2010824 (2021).
8. Chhetry, A. et al. Black phosphorus@laser-engraved graphene heterostructure-based temperature–strain hybridized sensor for electronic-skin applications. *Adv. Funct. Mater.* **31**, 2007661 (2021).
9. Lee, J. H. et al. Rational design of all resistive multifunctional sensors with stimulus discriminability. *Adv. Funct. Mater.* **32**, 2107570 (2022).
10. You, I. et al. Artificial multimodal receptors based on ion relaxation dynamics. *Science* **370**, 961–965 (2020).
11. Zhang, H. et al. Bioinspired chromotropic ionic skin with in-plane strain/temperature/pressure multimodal sensing and ultrahigh stimuli discriminability. *Adv. Funct. Mater.* **32**, 2208362 (2022).
12. Shin, Y. E. et al. Ultrasensitive multimodal tactile sensors with skin-inspired microstructures through localized ferroelectric polarization. *Adv. Sci.* **9**, 2105423 (2022).
13. Bae, G. Y. et al. Pressure/temperature sensing bimodal electronic skin with stimulus discriminability and linear sensitivity. *Adv. Mater.* **30**, 1803388 (2018).
14. Khonina, S. N., Kazanskiy, N. L., Butt, M. A. & Karpeev, S. V. Optical multiplexing techniques and their marriage for on-chip and optical fiber communication: a review. *Opto-Electron. Adv.* **5**, 210127 (2022).
15. Li, K. et al. Neurons in primate visual cortex alternate between responses to multiple stimuli in their receptive field. *Front. Comput. Neurosci.* **10**, 141 (2016).
16. Akam, T. & Kullmann, D. M. Oscillatory multiplexing of population codes for selective communication in the mammalian brain. *Nat. Rev. Neurosci.* **15**, 111–122 (2014).
17. Tallon-Baudry, C. The roles of gamma-band oscillatory synchrony in human visual cognition. *Front. Biosci.* **14**, 321–332 (2009).
18. Panzeri, S., Brunel, N., Logothetis, N. K. & Kayser, C. Sensory neural codes using multiplexed temporal scales. *Trends Neurosci.* **33**, 111–120 (2010).
19. Hoppensteadt, F. C. & Izhikevich, E. M. Thalamo-cortical interactions modeled by weakly connected oscillators: could the brain use FM radio principles?. *BioSystems* **48**, 85–94 (1998).
20. Caruso, V. C. et al. Single neurons may encode simultaneous stimuli by switching between activity patterns. *Nat. Commun.* **9**, 2715 (2018).
21. Kuzubasoglu, B. A. & Bahadir, S. K. Flexible temperature sensors: a review. *Sens. Actuators A Phys.* **315**, 112282 (2020).
22. Amjadi, M., Pichitpajongkit, A., Lee, S., Ryu, S. & Park, I. Highly stretchable and sensitive strain sensor based on silver nanowire–elastomer nanocomposite. *ACS Nano* **8**, 5154–5163 (2014).
23. Warkusz, F. The size effect and the temperature coefficient of resistance in thin films. *J. Phys. D: Appl. Phys.* **11**, 689 (1978).
24. Mohammad, B. et al. State of the art of metal oxide memristor devices. *Nanotechnol. Rev.* **5**, 311–329 (2016).
25. Shin, J. et al. Sensitive wearable temperature sensor with seamless monolithic integration. *Adv. Mater.* **32**, 1905527 (2020).
26. Van der Maaten, L. & Hinton, G. Visualizing data using *t*-SNE. *J. Mach. Learn. Res.* **9**, 2579–2605 (2008).
27. Tong, J., Mao, O. & Goldreich, D. Two-point orientation discrimination versus the traditional two-point test for tactile spatial acuity assessment. *Front. Hum. Neurosci.* **7**, 579 (2013).
28. Cho, S. et al. Wireless, multimodal sensors for continuous measurement of pressure, temperature, and hydration of patients in wheelchair. *npj Flex. Electron.* **7**, 8 (2023).
29. Mao, Q., Liao, Z., Yuan, J. & Zhu, R. Multimodal tactile sensing fused with vision for dexterous robotic housekeeping. *Nat. Commun.* **15**, 6871 (2024).
30. Won, S. M. et al. Multimodal sensing with a three-dimensional piezoresistive structure. *ACS Nano* **13**, 10972–10979 (2019).
31. Lee, D. & Bae, J. Soft multimodal sensors with decoupled multimodality and minimal wiring for wearable systems. *Adv. Funct. Mater.* **34**, 2409841 (2024).
32. Lyu, X. et al. Multi-modal sensing ionogels with tunable mechanical properties and environmental stability for aquatic and atmospheric environments. *Adv. Mater.* **36**, 2410572 (2024).
33. Tian, S., Wang, L. & Zhu, R. A flexible multimodal pulse sensor for wearable continuous blood pressure monitoring. *Mater. Horiz.* **11**, 2428–2437 (2024).
34. Chen, C. et al. Biomimetic multimodal receptors for comprehensive artificial human somatosensory system. *Adv. Mater.* **36**, 2313228 (2024).
35. Zhou, Y. et al. A multimodal magnetoelastic artificial skin for underwater haptic sensing. *Sci. Adv.* **10**, eadj8567 (2024).
36. Wang, S. et al. Flexible optoelectronic multimodal proximity/pressure/temperature sensors with low signal interference. *Adv. Mater.* **35**, 2304701 (2023).
37. Lee, B.-Y. et al. Human-inspired tactile perception system for real-time and multimodal detection of tactile stimuli. *Soft Robot.* **11**, 270–281 (2024).
38. Wang, Y. et al. Hierarchically patterned self-powered sensors for multifunctional tactile sensing. *Sci. Adv.* **6**, eabb9083 (2020).
39. Ma, M. et al. Self-powered flexible antibacterial tactile sensor based on triboelectric-piezoelectric-pyroelectric multi-effect coupling mechanism. *Nano Energy* **66**, 104105 (2019).
40. Shin, Y.-E. et al. Self-powered triboelectric/pyroelectric multimodal sensors with enhanced performances and decoupled multiple stimuli. *Nano Energy* **72**, 104671 (2020).
41. Wang, Y. et al. Cephalopod-inspired chromotropic ionic skin with rapid visual sensing capabilities to multiple stimuli. *ACS Nano* **15**, 3509–3521 (2021).
42. Shin, S.-H. et al. Ion-conductive self-healing hydrogels based on an interpenetrating polymer network for a multimodal sensor. *Chem. Eng J.* **371**, 452–460 (2019).
43. Guo, H. et al. Pro-healing zwitterionic skin sensor enables multi-indicator distinction and continuous real-time monitoring. *Adv. Funct. Mater.* **31**, 2106406 (2021).
44. Lei, Z. & Wu, P. A supramolecular biomimetic skin combining a wide spectrum of mechanical properties and multiple sensory capabilities. *Nat. Commun.* **9**, 1134 (2018).
45. Chen, L., Chang, X., Wang, H., Chen, J. & Zhu, Y. Stretchable and transparent multimodal electronic-skin sensors in detecting strain, temperature, and humidity. *Nano Energy* **96**, 107077 (2022).
46. Lo, L.-W. et al. A soft sponge sensor for multimodal sensing and distinguishing of pressure, strain, and temperature. *ACS Appl. Mater. Interfaces* **14**, 9570–9578 (2022).
47. Zhang, F., Zang, Y., Huang, D., Di, C.-A. & Zhu, D. Flexible and self-powered temperature–pressure dual-parameter sensors using microstructure-frame-supported organic thermoelectric materials. *Nat. Commun.* **6**, 8356 (2015).
48. Han, S. et al. Thermoelectric polymer aerogels for pressure–temperature sensing applications. *Adv. Funct. Mater.* **27**, 1703549 (2017).
49. Zhang, X. et al. High-performance multimodal smart textile for artificial sensation and health monitoring. *Nano Energy* **103**, 107778 (2022).

50. Park, J., Kim, M., Lee, Y., Lee, H. S. & Ko, H. Fingertip skin–inspired microstructured ferroelectric skins discriminate static/dynamic pressure and temperature stimuli. *Sci. Adv.* **1**, e1500661 (2015).
51. Rao, J. et al. Tactile electronic skin to simultaneously detect and distinguish between temperature and pressure based on a triboelectric nanogenerator. *Nano Energy* **75**, 105073 (2020).
52. Zhu, P. et al. A flexible active dual-parameter sensor for sensitive temperature and physiological signal monitoring via integrating thermoelectric and piezoelectric conversion. *J. Mater. Chem. A* **7**, 8258–8267 (2019).

Methods

AgNW synthesis

AgNWs were synthesized using a modified polyol method. Initially, 0.4 g of polyvinylpyrrolidone (M_w, ~360,000) and 0.5 g of silver nitrate ($AgNO_3$) were dissolved in 50 ml of ethylene glycol under magnetic stirring (300 rpm) for 30 min. Then, 800 µl of $CuCl_2{\cdot}2H_2O$ solution (3.3 mM in ethylene glycol) and 800 µl of $CuBr_2$ solution (1.68 mM in ethylene glycol) were pipetted into the solution. After ensuring complete dissolution of all substances, the magnetic stirrer was removed. The mixture was then heated to 150 °C and was maintained for 60 min until the solution became olive grey in colour. When the growth was finished, 200 ml of acetone was added to the resultant solution to aggregate AgNWs, and it was purified by dispersing in ethanol and centrifuging at 1,850*g* for 10 min. This purification process was repeated three times. For the electrode, the AgNW solution was redispersed in ethanol to a concentration of 0.1 mg ml^{-1}, and for the Ag@Cu_2O core–shell nanowire, the AgNW solution was redispersed in deionized water.

Synthesis of memristive Ag@Cu_2O core–shell nanowire

For the synthesis of Ag@Cu_2O core–shell nanowires, the methodology was adapted from previously established procedures for Au@Cu_2O core–shell nanomaterials, with certain modifications (Supplementary Fig. 22)[53]. The synthesis began by mixing 3 ml of the previously prepared AgNW solution, 1 ml of 0.01-M $CuCl_2$ solution, 0.8 ml of 0.45-M sodium dodecyl sulfate solution and 0.6 ml of 1-M NaOH solution in 28.7 ml of deionized water under magnetic stirring. After stirring for 3 min, 1.5 ml of 0.2-M $NH_2OH{\cdot}HCl$ solution was pipetted, and the Cu_2O shell grew for 10 min. The Ag@Cu_2O core–shell nanowires were cleaned using acetone via centrifugation at 450*g* for 10 min, then redispersed in ethanol and further cleaned through repeated centrifugation under the same conditions.

Fabrication of memristive multimodal receptor

The sensor fabrication involved several sequential steps. First, polydimethylsiloxane was spin coated onto a glass substrate and subsequently annealed. For electrode preparation, the AgNW solution was deposited using the vacuum filtration method. A pulsed ultraviolet laser system was then used for forming the sensing channel and cutting the sensor. In the first step, the laser ablated a 60-µm section of the AgNW electrode. This ablated channel was subsequently filled by repeated vacuum filtration of Ag@Cu_2O core–shell nanowires. Then, the sensor was achieved by cutting the polydimethylsiloxane substrate with the ultraviolet laser. A detailed schematic is provided in Supplementary Fig. 23.

Simulation modelling for a memristive nanowire network

To evaluate the electrical conductivity of a randomly dispersed nanowire network, the graphical theory approach is adopted (Supplementary Figs. 24 and 25)[54,55]. Our methodology involves the random percolation of 150 nanowires, onto a two-dimensional rectangular plane (60 µm × 60 µm). Subsequently, the adjacency matrix (A) and the incidence matrix (I) are derived for capturing the topology of the nanowire network. Edges represent the resistance of the nanowires and junctions, whereas nodes represent the percolation and potentials of each point. The correlation between the total current and total voltage across the entire network follows Ohm's law and Kirchhoff's law. Therefore, the total resistance can be calculated by the equation $Vi = L$ (L is Laplacian matrix $L = ICI^T$) with boundary conditions of input and output current flow at both ends of electrodes (i(o) = 1, i(N) = −1). Furthermore, a specific voltage is obtained by the gradient descent method. On the basis of this method, the behaviour of electrical resistance of the memristive nanowire network under a continuous voltage sweep is observed. In particular, only Ag–Cu_2O–Ag junctions have memristive properties, which are modelled by a power law incorporating the threshold voltage for filament growth. Graph theory is used to compute the potential gradient across all the nanowire network junctions, as outlined earlier. Each junction's current flow, which is backtracked by potential gradient and junction resistances, updates the electrical resistance of the Ag–Cu_2O–Ag junction. This process is repeated during the voltage sweep to monitor the resistance change behaviour (Supplementary Video 3).

Measurement of memristive properties and sensor response

A custom-made LabVIEW program (ver. 15.0.1) and source meter (SMU 2450, Keithley) were used for the measurement of memristive properties and sensor response. During the measurement, the pulse period, voltage and compliance current were precisely controlled. For the measurement of electrical signal during interaction with objects, a high-resolution linear actuator and a digital source meter were used. All experiments were performed in strict compliance with the guidelines of the Institutional Review Board (IRB) at Seoul National University (IRB number 2304/002-006).

Learning for object recognition

We used a sliding time window of size 32 across the data sequence; 32 frames of consecutive sensor values were regarded as a single input. A second-order low-pass Butterworth filter is applied to eliminate high-frequency noise and preserve relevant features. Moreover, to enhance the model's generalization, we applied data augmentation to the training set. This includes random scaling of the signal amplitude, with scaling factors in the range of $0.9 \leq \text{scale} \leq 1.1$. For pretraining, we divided the dataset into training and test subsets at an 8:2 ratio. During data preprocessing, min–max normalization was applied to the sensor signals to reduce environmental noise.

Our neural architecture features a six-layer LSTM network (encoder) and a three-layer dense network (decoder), with an input dimension of 2. Separate inputs accommodate interleaved signals from both M and T modes. Each frame from the 32-frame input was sequentially processed by LSTM units, resulting in a 128-dimensional hidden vector. Three trainable gates in each LSTM unit controlled information flow between the cells, preventing the gradient vanishing problem and enriching the information received by the dense layers. Then, the output of the LSTM is conveyed to the attention layer, to capture dependencies over the time window. The decoding network is composed of three layers of dense layers that finally predict the object classes.

Subsequently, the produced 128-dimensional vector is concatenated with the original input, forming a 192-dimensional vector, to preserve the original temporal information of the signal. A 30% dropout was applied across all the layers to prevent overfitting and a rectified linear unit served as the activation function for these layers. We implemented the network using the PyTorch deep learning framework, and the network was trained using the Adam optimizer with a learning rate of 10^{-4}. We used CrossEntropy as the loss function to train our network.

Data availability

The data supporting the findings of this study are available within the Article and its Supplementary Information. Additional data are available from the corresponding author upon request.

Code availability

The code that supports the results within this Article and the other findings of this study are available from the corresponding author upon request.

References

53. Zhu, S. et al. Synthesis of Au@Cu_2O core–shell nanoparticles with tunable shell thickness and their degradation mechanism in aqueous solutions. *Langmuir* **36**, 3386–3392 (2020).

54. Manning, H. G. et al. Emergence of winner-takes-all connectivity paths in random nanowire networks. *Nat. Commun.* **9**, 3219 (2018).
55. Hochstetter, J. et al. Avalanches and edge-of-chaos learning in neuromorphic nanowire networks. *Nat. Commun.* **12**, 4008 (2021).

Acknowledgements

This work was supported by the National Research Foundation of Korea (RS-2025-11092968) and the Air Force Office of Scientific Research (FA2386-24-1-4089).

Author contributions

K.K.K., J.B., M.K., I.H. and S.H.K. conceived and designed the study. K.K.K. and J.B. designed and performed the experiments. K.K.K. and J.B. developed the algorithms and analysed the data. J.B., K.K.K. and J.J. carried out the nanowire synthesis. K.K.K., J.B., M.K. and S.H.K. wrote the paper and incorporated comments and edits from all authors.

Competing interests

The authors declare no competing interests.

Additional information

Supplementary information The online version contains supplementary material available at https://doi.org/10.1038/s41563-025-02373-w.

Correspondence and requests for materials should be addressed to Seung Hwan Ko.

Peer review information *Nature Materials* thanks Xinyu Liu, Peiyi Wu and the other, anonymous, reviewer(s) for their contribution to the peer review of this work.